Slot-Die-Coating Operability Windows for Polymer Electrolyte Membrane Fuel Cell Cathode Catalyst Layers

Erin B. Creel[1], Kristianto Tjiptowidjojo[2], J. Alex Lee[3], Kelsey M. Livingston[1], P. Randall Schunk[2,4], Nelson S. Bell[4], Alexey Serov[1], and David L. Wood, III[1,*]

[1]Electrification and Energy Infrastructures Division,
Oak Ridge National Laboratory; Oak Ridge, TN 37831, USA

[2]Center for Micro-Engineered Materials,
University of New Mexico,
Albuquerque, NM 87131-0001, USA

[3]Saint-Gobain Research North America
Northborough, MA 01532, USA

[4]Sandia National Laboratories
Albuquerque, NM 87185- 0826, USA

*Corresponding Author

wooddl@ornl.gov

Keywords: proton exchange membrane fuel cell, gas diffusion electrode, slot-die coating, cathode catalyst layer, roll-to-roll manufacturing

Abstract

Roll-to-roll (R2R) slot-die coating of polymer electrolyte membrane fuel cell (PEMFC) catalyst layers represents a scalable deposition method for producing 10-20 $m^2 \cdot min^{-1}$ of catalyst-coated gas diffusion layers (GDLs). This high throughput production technique will help lower the cost of PEMFC catalyst layers. The uniformity of the wet layer applied by slot die deposition is affected

by process parameters such as substrate speed, vacuum pressure applied at the upstream meniscus, gap between the slot die lips and substrate, ink rheology, and other ink and substrate properties. The set of conditions for producing a defect-free coating with a dilute ink typically requires little to no upstream vacuum pressure, so suitable operating conditions can be found easily through trial and error and operator intuition. However, the higher viscosity of more concentrated inks dramatically shifts the range of settings that result in a homogeneous coating to higher vacuum levels, which are harder to find through hit or miss. A predictive model showing the range of operable conditions decreases material wastage inherent in experimentally searching for suitable parameters. In this study, the defect-free coating parameter window is explored experimentally and theoretically for two concentrations of PEFC cathode inks. Both a full capillary hydrodynamic model and a computationally cheaper viscocapillary model successfully predict the experimentally determined coating window within the experimental and model uncertainty limits for inks with 5.3 wt.% and 12.0 wt.% solids ink while maintaining the 0.1 $mg_{Pt} \cdot cm^{-2}$ United States Department of Energy (U.S. DOE) Pt areal loading target. This paper demonstrates a viable pathway for meeting the $\$30/kW_{net}$ ultimate cost target of the US DOE Hydrogen Fuel Cells Technologies Office (HFTO). The concentrated ink lowers the thermal energy and capital expenditure (CapEx) budget of the coating process by decreasing the amount of time, energy, and floorspace required for drying the coating.

1 Introduction

Polymer electrolyte membrane fuel cells (PEMFCs) are a promising, zero-tailpipe-emissions alternative to internal combustion engines due to high power density, low startup time, low operating temperature, and rapid load response.[1] However, PEMFCs remain cost-prohibitive despite the >10X reduction in PEMFC stack cost over the last three decades.[2] The costs of PEMFC stacks at the current volumes sold (several thousand vehicles per year worldwide[3]) are still at least three times higher than the United States Department of Energy (U.S. DOE) Hydrogen Fuel Cells Technologies Office (HFTO) ultimate target (i.e. $100/kW vs. $30/kW).[3,4] A primary reason for this difference is the processing costs and economies of scale of key repeating components such as gas diffusion electrodes (GDEs).[3] Spray coating, a commonly used catalyst layer deposition technique, requires dilute inks, suffers from spray nozzle clogging, and cannot meet the high throughput requirements for high PEMFC production volumes.[5–7] On the other hand, roll-to-roll (R2R) manufacturing —in which a flexible substrate is unwound, coated, dried, and re-wound— with continuous liquid film deposition helps to lower material and labor costs at an industrial scale through rapid, high-throughput, continuous, and highly-automated processing.

While several reliable deposition methods for R2R coating are available, including gravure, slot, and slide coating, this work focuses on slot die coating due to its ability to handle a wide range of coating ink viscosities and thicknesses. A slot die coating process, patented by Kodak in 1954[8] and diagramed in **Figure 1a**, consists of two parallel steel components forming a "slot" through which a coating fluid ("ink") is pumped. The edges of the blades ("die lips") are brought a short distance

(H_0) away from a moving substrate ("web") where a meniscus of fluid ("coating bead") is established and the ink is deposited in a thin film over the web. The slot die system pre-meters the volumetric coating fluid extrusion rate (Q_f). In conjunction with the roll-to-roll line speed (U) and cross-web coating width (w_{film}), Q_f allows for precise control of the wet thickness (t) of the coating (**Figure 1b**). w_{film} is easily controlled in slot-die coating with the use of a metal shim inserted between the blades of the slot die that sets the coating width. These factors make slot-die coating a highly versatile and low-waste coating technique for precise and uniform film application. While

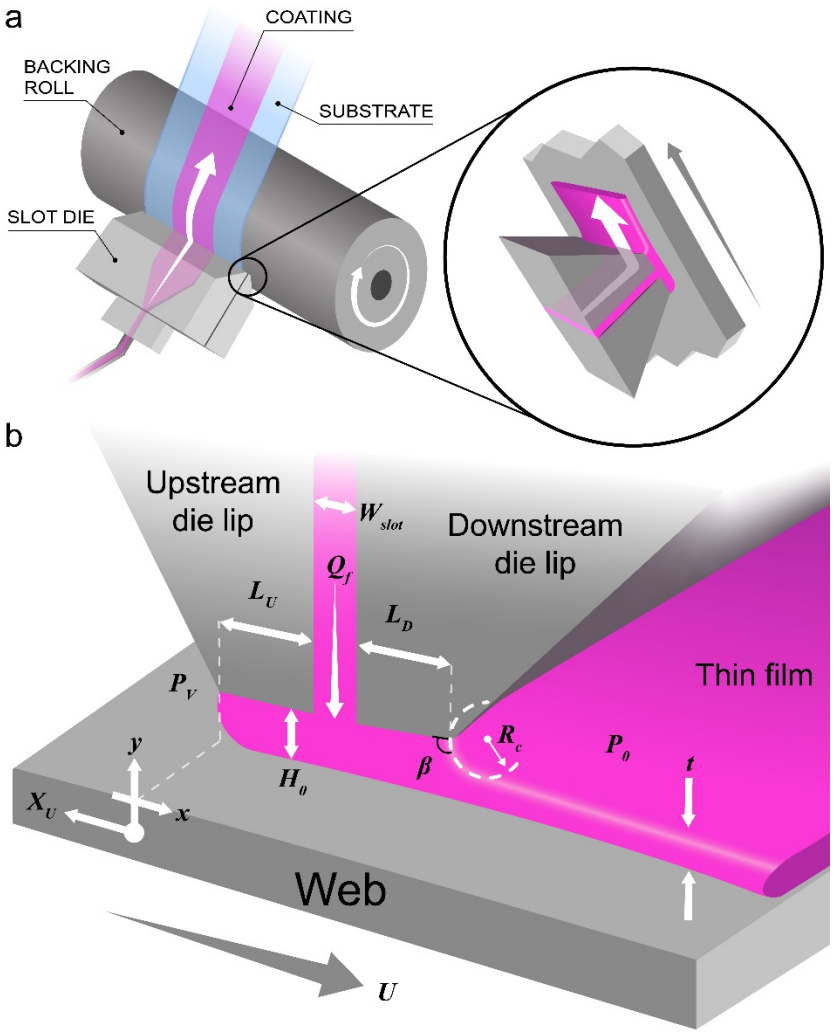

Figure 1. Roll-to-roll slot die schematics. a) Diagram of the slot die application of a coating to a substrate with inset showing the coating bead detail. b) Diagram of the slot die coating bead and the relevant parameters for the computational models.

78 slot-die coating is a commonly used technique in applications such as photographic film,[8,9] flexible
79 organic photovoltaics,[10–14] transparent conductive films,[15–17], battery electrodes,[18–21] and other
80 electronic devices,[22–25] there are few open literature examples of slot-die coating for deposition of
81 the catalyst layer for PEMFCs.[7,26,27]
82
83 In this paper, we demonstrate R2R deposition of the Pt, C, and ionomer cathode catalyst layer for
84 a PEMFC using two ink formulations. The catalyst layers are applied onto a microporous layer
85 (MPL)-coated gas diffusion layer (GDL) to make a GDE. MPL-GDLs are flexible, allowing them
86 to travel around the rollers in a R2R coating system, and do not warp when wet, making them well-
87 suited for slot coating. Continuous liquid film deposition with R2R modalities enables GDEs to be
88 produced without the challenges of spray coating such as nozzle clogging and limitations on ink
89 solids-loadings (<<1 wt.% for spraying vs. >5 wt.% for R2R deposition). Increasing the solids-
90 loading of an ink decreases the mass of dispersion media (made of water and alcohol solvents)
91 needed per unit area of coating, decreasing both the expenditures on dispersion media and the
92 energy needed to dry the coating. Decreasing energy consumption in manufacturing sectors has
93 been a priority of the U.S. DOE Advanced Manufacturing Office (AMO) because manufacturing
94 uses about 20 % of the nation's energy.[28] Importantly, decreasing the dispersion media content of
95 a system and making the dispersion media more water-rich decreases both the environmental and
96 human health impacts of the process. In fact, this satisfies six of the Twelve Principles of Green
97 Chemistry: 1) waste prevention, 3) less hazardous chemical synthesis, 5) safer solvents and
98 auxiliaries, 6) design for energy efficiency, 7) use of renewable feedstocks, and 12) inherently
99 safer chemistry for accident prevention.[29] Alcohols such as 1-propanol that are sometimes used as
100 the majority component of dispersion media in low-temperature PEMFC catalyst layers are

flammable, petroleum-derived, and toxic to humans. Water, on the other hand, is a benign and sustainable solvent. However, water is also more difficult to remove in the solidification process due to its higher boiling point.

Increasing the proportion of water in the dispersion media system also benefits the PEMFC performance. Water-rich catalyst layer ink formulations decrease ionomer aggregate size and improve interactions between the ionomer sulfonate groups and the Pt catalyst due to the polarity of the water molecules. Therefore, PEMFC catalyst layers made from water-rich inks exhibit decreased ionic transport resistance in the ionomer film relative to a catalyst layer made from an n-propanol-rich ink. Some alcohol content is needed to improve ink coatability, catalyst dispersion, and mitigate the increased resistance at the Pt/ionomer interface due to the strength of interaction in water-rich systems.[30,31] The inks used in this study have water/1-propanol mass ratios of 2.5-3.0.

In this study, dilute and concentrated catalyst inks were coated by R2R slot-die onto an MPL-GDL with the coating parameters guided by analytical and computational model predictions. Each ink was coated at a variety of web speeds and upstream vacuum pressures (pressure difference between ambient air pressure downstream of the slot die and air pressure in the vacuum box behind the upstream meniscus) to test the predicted coating window limits. Wet thicknesses, t_{wet}, were adjusted for each ink formulation to ensure the desired cathode Pt loading of 0.1 $mg_{Pt} \cdot cm^{-2}$. The dilute ink required a higher t_{wet} than the concentrated ink. The two mathematical models used to predict the coating window are a less computationally expensive viscocapillary model in Matlab

and a more computationally expensive finite element model (FEM) using the open-source software package Goma 6.0.[32]

Both models use predicted location of upstream meniscus as the basis of coating window determination. The viscocapillary model is based on the lubrication approximation which reduces the problem to one-dimension. The Goma 6.0 model, on the other hand, solves the complete Navier-Stokes equations and treats the whole flow domain as two-dimensional, thereby making it a more rigorous flow model. Both models successfully predicted the experimentally determined coating windows within 200Pa of applied backpressure for both the dilute and concentrated inks. Thus, this study demonstrates that the defect-free slot-die coating window can be predicted for low- and high-solids-loading PEMFC cathode layer inks effectively, thereby leading to significant savings of material and time while conducting coating trials.

2 Materials and Methods

2.1 Catalyst Ink Preparation

Catalyst inks were prepared by adding the appropriate mass of Pt on high surface area carbon (Pt/HSC) catalyst powder (Tanaka Kikinzoku Kogyo, 47.0 wt.% Pt, TEC10E50E) followed by the appropriate mass of deionized water to a 500 mL capacity Nalgene jar. The mixture was swirled by hand to disperse the catalyst powder in the water. **WARNING:** It is important that the water and catalyst powder are mixed before any alcohol is added because Pt/HSC may spontaneously combust with addition of alcohol if insufficient water is present. The appropriate mass of 21 ± 1 wt.% of 1000 equivalent weight (EW) Nafion in 34 ± 2 wt.% water, 44 ± 2 wt.% 1-propanol, and

145 < 2 wt.% ethanol (Fuel Cell Store, Nafion Dispersion D2020) was added to the jar followed by
146 more swirling by hand. Finally, the appropriate mass of 1-propanol (Sigma-Aldrich, ≥ 99.5 %)
147 was added to the mixture. Formulation information for the inks can be found in **Table 1**. Next,
148 mechanical mixing was completed at 10,000 rpm in the jar for 1 h on a high shear mixer (IKA,
149 T25 Digital S1, 115 V) with a rotor-stator attachment (IKA, S25N-18G) to deagglomerate catalyst
150 particles and disperse all components. The ink was stirred with a magnetic stir bar on a stir plate
151 at 300 rpm overnight prior to application to allow any foam generated during mixing to dissipate.
152
153 **Table 1.** Composition of catalyst ink with respect to the total ink mass.

	Dilute Ink	Concentrated Ink
Component		
Pt/HSC (wt.%)	3.50	8.00
Water (wt.%)	68.40	56.27
Nafion D2020 solution (wt.%)	8.47	19.17
1-propanol (wt.%)	19.63	16.57
Total Formulation Descriptors		
Total Solid Content (wt.%)	5.28	12.02
Ionomer to carbon quotient (I/C)	0.96	0.95
Water:1-propanol (by mass)	77:23	71:29

154

155 ## 2.2 Catalyst Layer Preparation and R2R Coating

156 The catalyst inks were coated by slot die onto two substrates, an MPL-GDL and an untreated
157 aluminum foil. The GDL was a 230 μm thick carbon paper with a hydrophobic MPL coating
158 (Freudenberg, H23C8). The thickness of the MPL-GDL was measured with a 690 nm red optical
159 laser caliper with a spot size of 25 μm at 1 μm intervals over a 1.6 m length of the substrate. The
160 catalyst ink was deposited onto the substrate by a single layer slot die (Allied Dies, AD-1992)
161 equipped with a 127 μm (0.005 in.) thick shim with an opening for a 7.6 cm (3 in.) wide coating.

The stainless steel slot die was mounted at 25° below horizontal on a backing roll with 1.3 μm total indicator runout (T.I.R.) (**Figure S1, Supporting Information**). Both upstream and downstream die lip lengths (L_u and L_D) are 813 μm (0.032 in.) The substrate was translated across the face of the die lips at web speeds varying from 0.6-2.7 $m \cdot min^{-1}$ (2-9 $ft \cdot min^{-1}$) and dried using roll-to-roll coating machine with a seven-zone drying oven (Frontier Industrial Technology, DynaCoat CEB-355). The coating was dried in a heating zone consisting of seven convection ovens in series at 32, 37, 42, 47, 52, 47, and 42 °C (90, 99, 108, 117, 126, 117, 108 °F), respectively. The ink was extruded out of an oil displacer tube that mitigates any pulsation of the "pulse-free" digital gear micropump (Cole-Parmer Masterflex L/S Model no. 75211-70).

2.3 Catalyst Ink Characterization

2.3.1 Ink Rheology

Shear viscosity measurements were collected at 25 °C with two different rheometer methods to ensure repeatability. The shear viscosity profile measured on the concentrated ink changed with the rheology method. Concentrated ink, "Viscosity 1" was measured using a Haake MARS II stress-controlled rheometer equipped with a C60 Ti (1°) cone and plate sensor with a tip gap distance of 52 μm. A solvent trap was used to prevent liquid evaporation during the measurement, and the software was operated in rate-controlled mode. Pre-shear was conducted at 500 /s for 120 s, followed by a quiescent rest period of 120 s under no applied stress. Shear rate sweeps from 0.01 to 1000 /s were performed with a 300-s ramp, a 60-s hold at high shear, and a falling ramp to 0.1 /s in 300 s to complete a hysteresis loop. Three repetitions of the shear rate sweep were conducted to establish drift and reproducibility. No variance was noted between the tests. The average of the forward and back sweeps is reported in this paper.

Concentrated ink, "Viscosity 2" was measured using a TA Instruments Discovery HR-3 rheometer equipped with a concentric cylinder and conical rotor with 26.05 mm diameter and 42.01 mm length. The ink reservoir was covered to minimize solvent evaporation. Pre-shear was conducted at 0.8 /s for 60 s followed by a quiescent rest period of 60 s under no applied stress. Shear rate sweeps from 0.001 to 200 /s were performed with a 480 s ramp. Two repetitions were measured to establish reproducibility. The first measurement is reported in this paper.

The shear viscosity profile measured using the two methods for the dilute ink was very similar; we report the data collected from the "Viscosity 1" method.

2.3.2 Ink Surface Tension

The equilibrium surface tension of the inks was measured by the pendant drop method. A 2.2 mm outside diameter needle was large enough to make a 2-μL formed drop drip into a Laplacean shape (drip-like with a shape governed only by surface tension and density). In the case of the viscous concentrated ink, we placed a 50/50 water/propanol solution inside the sample chamber where the drop was pendant. With the solution in place to saturate the gas space environment around the drop we could wait up to five minutes to allow any given drop to reach an equilibrium condition. The pendant drop is digitally imaged using a high pixel charge-coupled device (CCD) camera. The drop's image is then fit by a robust mathematical approach to determine the drop's mean curvature at over 300 points along its surface. Using the ink density—0.981 $g \cdot mL^{-1}$ for the dilute ink and 0.984 $g \cdot mL^{-1}$ for the concentrated ink—an average of the surface tension calculated at each of these points determines

the surface tension of the liquid. We report the average surface tension in a five-drop experiment.

2.3.3 Ink Sessile Drop Contact Angle Measurements on Substrates

Static sessile drop contact angle measurements were made for five to ten 2-µL drops of ink on aluminum foil, MPL-GDL, and poly(tetrafluoroethylene) (PTFE) with an equilibration period of five minutes from the time the drop is incident on the surface. Dynamic contact angle increases with coating speed from the lower bound value, the static contact angle. The measured static contact angles of the ink on the aluminum foil and MPL-GDL substrates were used as a lower bound to inform the dynamic contact angle used in the Goma mathematical model. 120 ° was selected as a reasonable and convenient value for a macroscopic dynamic contact angle. The contact angle on the aluminum foil was used as the contact angle of the ink on the stainless steel die face and lips in the Goma model, a valid approximation due to the similarity in surface energy of aluminum foil and stainless steel. The ink contact angles on the PTFE substrate were used in combination with their surface tensions to calculate the dispersive and polar components of the surface tension. The surface energy and polarity of the aluminum foil and MPL-GDL substrate were calculated using the data from contact angle measurements of water and diiodomethane on the two surfaces.

3 Results and Discussion

3.1 Catalyst Ink and Substrate Characterization

3.1.1 *Catalyst Ink Surface Tension Characterization*

The so-called wettability of the substrate is governed primarily by the surface tension of the fluid and the contact angle of the fluid on the substrate. Liquids with lower surface tension tend to wet more easily as gravity works to spread out the fluid. The surface tension of a liquid, σ_L, stems from

the polar (dipole) and dispersive (van der Waals) interactions between the components of the fluid. The surface tensions of the dilute and concentrated inks (**Table 2**) were measured by pendant drop shape analysis and divided into polar and dispersive components using contact angle measurements on PTFE and Fowkes surface energy theory[33]. Though the inks have similar composition, differing primarily in their solids content, the dilute ink has a slightly lower polar component, leading to lower total surface tension.

Table 2. Catalyst ink optical tensiometry

	Dilute Ink	**Concentrated Ink**
Surface tension ($mN \cdot m^{-1}$)	41.81 ± 0.02	45.57 ± 0.02
Polar component ($mN \cdot m^{-1}$)	15.46	18.90
Dispersive component ($mN \cdot m^{-1}$)	26.35	26.67
Surface polarity (%)	36.97	41.47
Contact angle on PTFE (°)	87.6	92.2
Contact angle on foil (°)	38.7	46.5
Contact angle on MPL-GDL (°)	104.9	107.3

3.1.2 *Substrate Surface Energy Characterization*

The two substrates deployed for coating trials in this study are the aluminum foil and an MPL-GDL, which have substantially different surface energy properties. Surface energy is the solid analog to surface tension for liquids. The polar and dispersive components of the solid's surface energy can be determined using the Fowkes equation and the contact angles between the solid and liquids with known surface tension components.[33] Diiodomethane, a completely dispersive liquid, and water were used as probe liquids to determine the surface energy of the foil and MPL-GDL substrates.

Table 3 shows the water and diiodomethane contact angles, the surface energy, and the polar and dispersive components for aluminum foil and MPL-GDL. The MPL is a nonpolar hydrophobic coating on the GDL, so it is not surprising that the surface energy and especially the polar component of the surface energy of the MPL-GDL is very low. Aluminum foil has a higher surface energy but still has a lower surface polarity than the catalyst inks.

Table 3. Substrate optical tensiometry

	Aluminum Foil	**MPL-GDL**
Water contact angle (°)	76.3	146.8
Diiodomethane contact angle (°)	62.6	109.6
Surface energy ($mJ \cdot m^{-2}$)	34.28	6.44
Polar component ($mJ \cdot m^{-2}$)	7.20	0.84
Dispersive component ($mJ \cdot m^{-2}$)	27.08	5.61
Surface polarity (%)	21.01	12.97

Static contact angles measured for each ink on the two substrates (**Table 2**) show that the wettability of aluminum foil is much higher than the low-surface-energy MPL-GDL. In fact, inks are considered non-wetting on the MPL-GDL because the contact angle is >90 °. This behavior is expected because of the higher surface energy of the aluminum foil that makes wetting more thermodynamically favorable. Aluminum foil was used as the primary substrate for model validation experiments to eliminate any effects of the non-wetting ink. The MPL-GDL was also coated to create a full GDE and validate the models on a more practical substrate for PEMFCs.

3.1.3 *Substrate Thickness Characterization*

The MPL-GDL used in this study is a popular porous support for catalyst layers in fabricating GDEs. The manufacturer provides the thickness of the MPL-GDL, 230 or 200 μm, at 0.025 or 1

MPa, respectively. However, the specifications do not indicate the magnitude of the variation in thickness. The variation in thickness measured by a laser caliper over a 1.6 m piece of the MPL-GDL is more than 60 μm (**Figure 2**), which is equal to the wet thickness of the catalyst layer deposited from the dilute ink and twice that of the concentrated ink. For comparison, the variation in thickness of the aluminum foil and the backing roll runout are both 1 μm. The gap, H_0, between the die and the substrate in roll-to-roll slot die coating is generally set between 1.5 and 2 times the desired wet thickness. With a variation in substrate thickness the same order of magnitude as the wet thickness and the gap, the die could crash into the substrate at thick regions of the substrate. Additionally, the coating window is very sensitive to the size of the gap. If the gap is too small, then the ink can wet outside shoulder of the downstream die lip, leading to coating instabilities.[26,34] Aluminum foil with a thickness of 16 ± 1 μm (manufacturer-provided specifications) was used to verify the coating window predictions on a more uniform substrate before determining whether the predictions were still valid on the challenging MPL-GDL substrate.

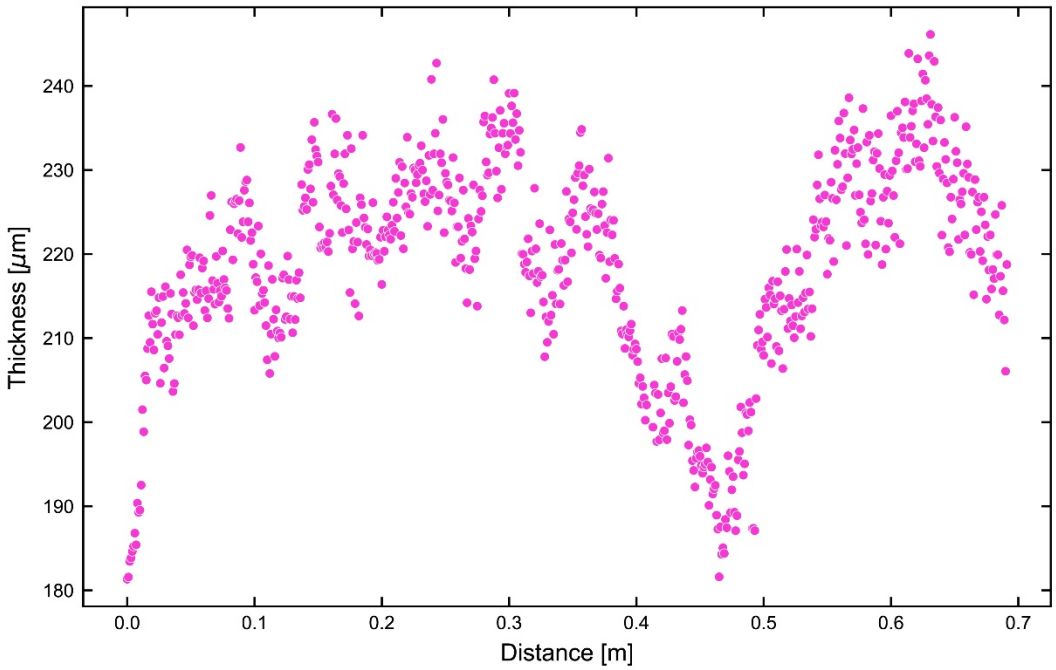

Figure 2. Thickness profile of the MPL-GDL along the coating direction as measured in one measurement by a laser caliper. The linearity of the instrument is ±1.2 µm.

3.1.4 *Catalyst Ink Rheology*

Ink rheology plays a key role in the vacuum operability limits of slot die coating.[35] It is necessary to characterize the full shear rate dependence of viscosity to properly account for the range of shear rates observed with the FEM of the coating process (100 – 1500 /s in this study). Concentrated Pt/HSC inks are particularly susceptible to particle agglomeration or ionomer relaxation which may result in large viscosity variations. Thus, the conditions selected for rheology measurements are of upmost importance. We aim to measure the rheology of the ink under conditions most similar to those during coating. The shear-mixed ink is stirred by magnetic bar overnight to remove foam before coating, so rheology is measured after bar mixing. The measurement technique can also impact the viscosity/shear-rate profile. For example, when the same concentrated ink is redispersed with different protocols (vortex mixing vs. bottle inversion), measured with or without

288 a solvent trap, measured with different pre-shear conditions (0.8 /s vs. 500 /s), and measured with
289 different rheometer geometries (cone and plate versus cup and bob), the shear viscosity
290 measurements differ by a factor of ~3 (Viscosity 1 vs. Viscosity 2, Table 4). The shear viscosity
291 profile of the dilute ink does not vary significantly with these choices in preparation and
292 measurement technique. **Figure 3a** shows the comparison of the shear viscosity profiles of the two
293 measurement techniques on the concentrated ink with that of the dilute ink.
294

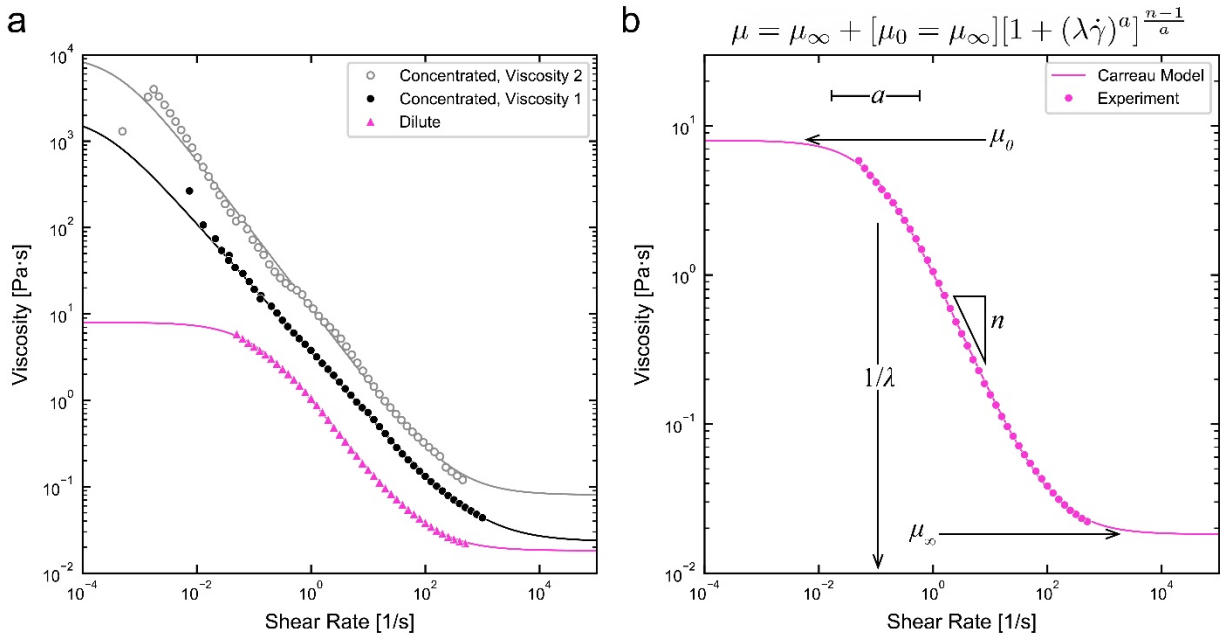

Figure 3. Shear viscosity profiles for the two catalyst inks, concentrated and dilute, used in this study. a) Comparison of the measured viscosity (dots) and Carreau-Yasuda rheology model fits (lines) for the dilute and concentrated inks. The viscosity of the concentrated ink depends on the measurement conditions (Viscosity 1, Viscosity 2). The dilute ink and concentrated ink, Viscosity 1 are the average of a forward and reverse scan. The concentrated ink, Viscosity 2 is a single forward measurement. b) Illustration of the significance of each of the Carreau-Yasuda rheology model parameters using the dilute ink data.

295

296 Increasing the solids loading from 5 wt.% to 12 wt.% for these PEMFC cathode inks increases the
297 viscosity by approximately an order of magnitude. The shear thinning behavior of both inks can
298 be explained by the flow-induced breakup of agglomerates of Pt/HSC catalyst particles.[36] The

shear viscosity profile of each ink is fitted with the Carreau-Yasuda viscosity model (**Figure 3a**, **Equation 1**). The Carreau-Yasuda model and the fitting parameters are used in both the viscocapillary and finite element computational models to determine the operability window. The Carreau-Yasuda model, which can describe shear thinning or shear thickening fluids, is

$$\mu = \mu_\infty + [\mu_0 - \mu_\infty][1 + (\lambda\dot{\gamma})^a]^{\frac{n-1}{a}} \quad (1)$$

where μ_0 and μ_∞ represent the viscosity at zero and infinite shear rate, λ is the relaxation time, and a is a transition parameter measuring the range of shear rates over which viscosity transitions from Newtonian at the low shear rate limit to the power law. These parameters are illustrated in a shear viscosity plot of dilute ink in **Figure 3b**. **Table 4** gives the Carreau-Yasuda rheology model fitting parameters for each ink. The zero-shear plateau viscosity, μ_0, for the concentrated inks is not clear, so multiple values for μ_0 will be considered in a sensitivity analysis for the operability window.

Table 4. Carreau-Yasuda rheological model fitting parameters.

Measurement Techniques	**Dilute Ink**	**Concentrated Ink, Viscosity 1**	**Concentrated Ink, Viscosity 2**
Ink redispersion method		Vortex mixing	Bottle inversion
Pre-shear rate (1/s)		500	0.8
Solvent trap?		Yes	No
Rheometer geometry		Cone and plate	Cup and bob
Rheological Fitting Parameter			
Zero shear viscosity, $\boldsymbol{\mu_0}$ [Pa·s]	8	2×10^3	1×10^4
Infinite shear viscosity, $\boldsymbol{\mu_\infty}$ [Pa·s]	1.82×10^{-2}	2.32×10^{-2}	8.03×10^{-2}
Power law index, n	0.117	0.254	0.136
Relaxation time, $\boldsymbol{\lambda}$ [s]	9.29	4.77×10^3	2.52×10^3
Transition parameter, a [mN·m^{-1}]	0.945	1	1

3.2 Mathematical Coating Window Models

For each coating liquid, target wet film thickness, and slot-die-web gap, defect-free coatings may be made within a limited window in the two-dimensional parameter space of upstream vacuum pressure and coating line speed. As a first approximation, this window can be bound by the so-called vacuum operability limits. Too high a vacuum pressure pulls the upstream coating bead too far out from under the die lips, while too low a vacuum pressure can result in the upstream coating bead being sucked in under the feed slot as illustrated in **Figure 4a**. Vacuum operability limits are defined as conditions where the upstream meniscus sits exactly at the extreme corners of the upstream die lip in steady operation. A diagram of a typical vacuum vs. line speed coating window is shown in **Figure 4a**. The high and low vacuum limits are predicted by the modeled position of the upstream meniscus. In this study, we compare two models that predict the high and low vacuum limits.

Vacuum operability limits are not true stability limits as they do not predict specific instabilities or defects, but some typical defects can be attributed to operating outside these limits (**Figure 4b**). Ribbing is a cross-web thickness undulation resulting from viscous forces being larger than can be counteracted by the downstream meniscus' capillary forces, 2) rivulets are alternating coated and uncoated stripes in the cross-web direction, and 3) barring is variation of coating thickness in the down-web direction.[21,34,35,37]. Below the low vacuum limit (too little vacuum), the upstream meniscus can recede under and invade the feed slot at high enough speeds, resulting in rivulets.[37] Above the high vacuum limit (too much vacuum) the upstream meniscus will be pulled out past the upstream lip corner, possibly resulting in swelling and weeping of the upstream meniscus and

ribbing and rivulet coating defects. The region of the coating parameter space between the minimum and maximum vacuum levels is the vacuum operability window, or coating window. Respecting the vacuum limits does not ensure defect-free coating at the coating head; for example, the so-called low flow limit will set another operability limit on the speed (rather than the vacuum) in the window of vacuum pressure vs line speed.[38] Moreover, avoiding defects at the coating head

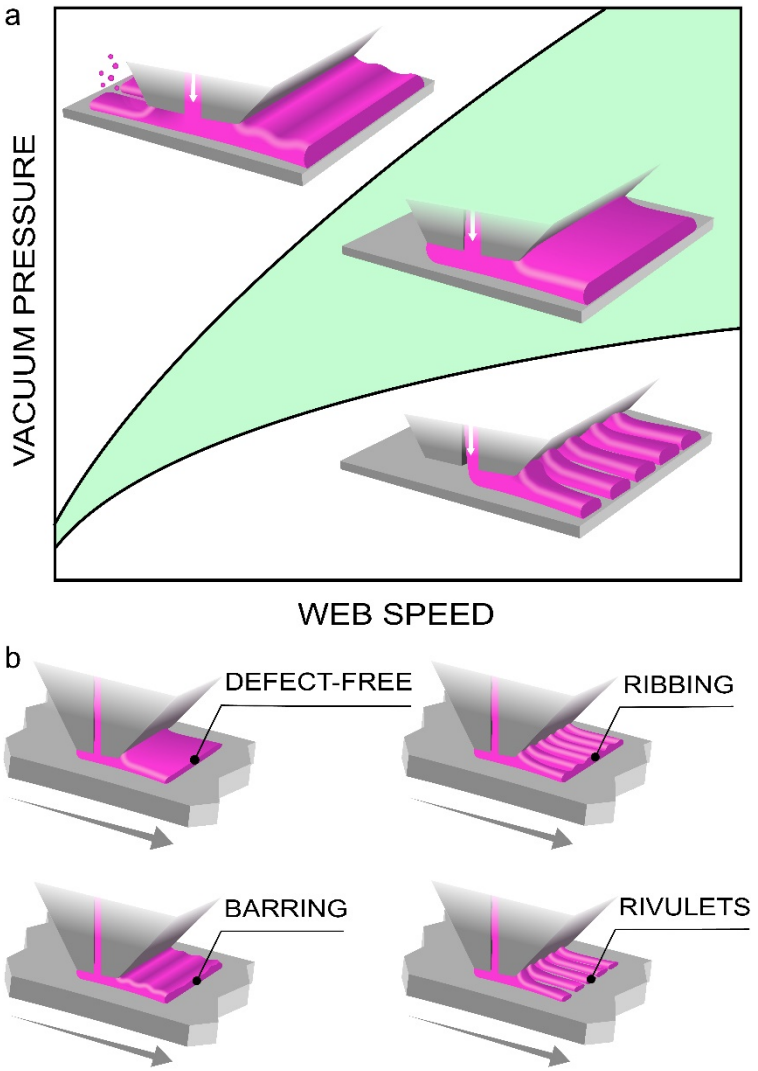

Figure 4. Graphics of a typical coating window and possible defects when operating outside the coating window as originally proposed by Sartor.[33] a) Typical defect-free operating window of line speed and vacuum pressures indicated in green. The changes to the coating bead if the vacuum level is too low or too high are illustrated in the graphics below and above the coating window region, respectively. b) Defect-free coating produced inside the operability window and coating defects that occur when operating outside the window.

does not preclude defects in the finished film product due to defects formed in drying and solidification.

In this study of PEMFC catalyst inks, we set the die-substrate gap, H_0, constant at 150 μm. Because we keep the Pt areal loading constant (0.1 $mg_{Pt} \cdot cm^{-2}$) in the final dried film, the wet thickness, t_{wet}, is different for each ink concentration. The wet thickness is set at 60 μm for the dilute ink and 30 μm for the concentrated ink. Because both the shear viscosity profile and wet thicknesses are different, an experimentally determined coating window for one ink is not expected to translate to the other. Moreover, it is not known a priori what the coating window should be for either ink. Therefore, we require some modeling of the coating bead to predict the vacuum operability limits.

3.2.1 Goma Finite Element Model

A modeling approach of using FEM to solve for equations governing slot coating flow has been presented by others.[34,38,39] Here we present a summary for completion. Slot-die coating flow is governed by a system of partial differential equations describing conservation of mass and momentum:

$$\underline{\nabla} \cdot \underline{\boldsymbol{v}} = 0 \tag{2a}$$

$$\rho\, \underline{\boldsymbol{v}} \cdot \underline{\nabla \boldsymbol{v}} = \underline{\nabla} \nabla \cdot \underline{\boldsymbol{T}} \tag{2b}$$

where $\underline{\boldsymbol{v}}$ is the velocity field, ρ is the liquid density, and $\underline{\boldsymbol{T}}$ is the total stress tensor, which for a generalized Newtonian liquid is $\underline{\boldsymbol{T}} = -\underline{\boldsymbol{I}} p + \mu\left[\nabla \underline{\boldsymbol{v}} + \nabla \underline{\boldsymbol{v}}^{\mathrm{T}}\right]$. $\underline{\boldsymbol{I}}$ is the identity tensor, p is pressure, and μ is viscosity. The dependence of μ on shear rate is given by the Carreau-Yasuda model, **Equation 1**. The differential equations are subject to boundary conditions as follows:

1. At the inflow plane, ideally we impose a fully developed velocity profile, i.e. $\boldsymbol{v_y} = f(x)$. However, the analytical form of the profile is not available for Carreau-Yasuda liquids. Instead, we impose a plug flow profile, i.e. $v_y = {Q_f}/{W_{\text{slot}}}$, in the expectation that it would evolve into its fully developed profile further downstream. W_{slot} is the feed slot opening width and Q_f is the volumetric flow rate per unit width, which can be obtained by multiplying web speed U and coating thickness t : $Q_f = Ut$. Here, we place the inflow plane 1 mm (~10 slot widths) away from the slot exit which is more than adequate to ensure fully developed flow prior to reaching the exit.
2. At the slot-die surface, the no slip velocity applies: $\underline{\boldsymbol{v}} = \underline{\mathbf{0}}$.
3. At the substrate surface, the no slip also applies: $\underline{\boldsymbol{v}} = \underline{\boldsymbol{t}}_w U$, except at the vicinity of the Dynamic Contact Line (DCL) where slip occurs: $\underline{\boldsymbol{t}}_w \underline{\boldsymbol{n}}_{\boldsymbol{w}}$: $\underline{\boldsymbol{T}} = {1}/{\beta}\left(\underline{\boldsymbol{t}}_{\boldsymbol{w}} \cdot \underline{\boldsymbol{v}} - U\right)$is the tangent vector at the web, $\underline{\boldsymbol{n}}_{\boldsymbol{w}}$ is the outward-pointing normal vector from the web at the liquid boundary, and β is the slip coefficient, in which its sensitivity to the predicted solution is presented later.
4. At the downstream meniscus, liquid traction is balanced with capillary pressure jump: $\underline{\boldsymbol{n}} \cdot \underline{\boldsymbol{T}} = 2H\sigma\underline{\boldsymbol{n}} - P_0$. $2H = {1}/{R_c}$ is the curvature of the meniscus, $\underline{\boldsymbol{n}}$ is normal to the free surface, σ is surface tension, and P_0 is the external pressure which is taken to be atmospheric pressure.
5. At the upstream meniscus, the traction balance also applies but with the external pressure equal to applied vacuum pressure instead: $\underline{\boldsymbol{n}} \cdot \underline{\boldsymbol{T}} = 2H\sigma\underline{\boldsymbol{n}} - P_V\underline{\boldsymbol{n}}$.
6. At the outflow plane, the film is fully developed such that its velocity gradient is invariant in the outflow direction: $\underline{\boldsymbol{n}} \cdot \underline{\nabla \boldsymbol{v}} = \underline{\mathbf{0}}$. The plane needs to be placed far enough downstream

to allow for the film flow to be fully developed. In this case, we place it 5 mm (~10 die-web gaps) away from the edge of downstream die lip and find it to be more than adequate.

The partial differential equations and the boundary conditions are solved with Galerkin FEM using Goma 6.0.[32] Complications arise from liquid-air menisci because their shapes are not known a priori and need to be solved as part of the equation system. Liquid-air menisci are handled by using the Arbitrary Lagrangian Eulerian method. This method deforms the finite element mesh to conform to the flow boundaries, including the menisci. The mesh deformation is treated as a pseudo-solid, which requires solving additional partial differential equation system as presented by Sackinger et al.[40] These additional equations are subject to another set of boundary conditions pertaining to flow geometry:

1. At the slot-die and substrate surfaces, the mesh location can be prescribed, i.e. $f(x,y) = 0$.
2. At the upstream and downstream menisci, the kinematic condition applies: $\underline{\boldsymbol{n}} \cdot \underline{\boldsymbol{v}} = 0$.
3. At the termination of the upstream meniscus, the positions of the upstream Static Contact Line (SCL_{up}) and DCL are not set directly, but rather the static contact angle (SCA) (θ_{SCA}) and dynamic contact angle θ_{DCA}) respectively are prescribed. Unlike the value of θ_{SCA} , which is a function of the liquid and solid properties alone (determined by contact angle measurement), the value of θ_{DCA} depends on the flow condition as well. Therefore, its sensitivity on the predicted solution is presented later.
4. At the termination of the downstream meniscus, the downstream Static Contact Line (SCL_{down}) is assumed to be pinned at the die corner; therefore, its location is fixed.

As stated in Section 3.2, vacuum limits are determined based on the location of the upstream meniscus. We solve for the values of applied vacuum pressure, p_{vac}, at those limits by adding another equation or constraint in the system. For high vacuum limits, we set the $\mathrm{SCL_{up}}$ position $x_{\mathrm{SCL}} = 0$, the upstream limit of the upstream die lip (**Figure 1**). For low vacuum limits, we set the DCL position $x_{\mathrm{DCL}} = L_u$, the downstream limit of the upstream die lip (**Figure 1**). **Figure S2 (Supporting Information)** shows flow fields at high and low vacuum limits.

Figure 5a shows the Goma prediction of the vacuum limits for slot die coating the dilute ink. As the measured shear viscosity profile of the concentrated ink varies with rheology preparation technique, a coating window was predicted for both viscosity profiles measured on the same ink.

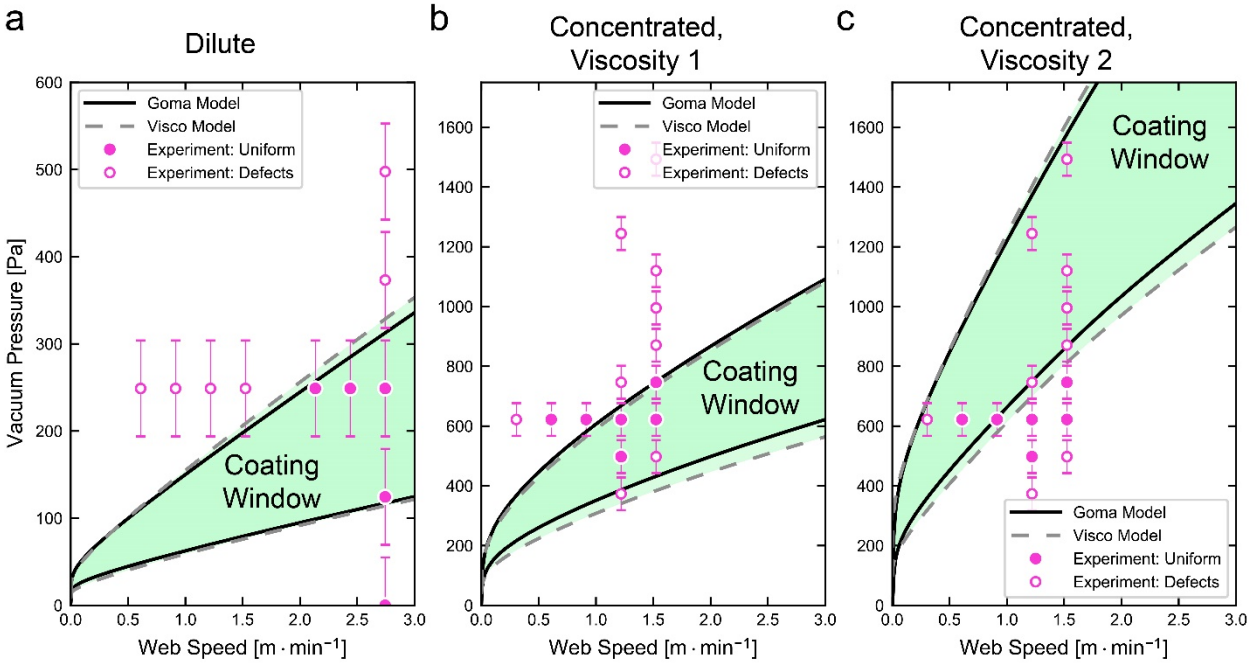

Figure 5. Predicted and experimental defect-free slot die vacuum-web speed operability windows for the catalyst inks coated on aluminum foil with a die-web gap of 150 µm. Goma predictions are given by solid lines. Viscocapillary predictions are given by dashed lines. Closed circles indicate an experimentally defect-free coating for 0.5 m or more. Open circles indicate an experimentally defected coating for 0.5 m or more. Experimental error bars indicate the uncertainty in the vacuum gauge. a) Coating window for dilute ink with a wet thickness of 60 µm. b) Coating window for concentrated ink, Viscosity 1 with a wet thickness of 30 µm. c) Coating window for concentrated ink, Viscosity 2 with a wet thickness of 30 µm.

418 The model is sensitive to the ink rheology, so the predicted operability windows differ significantly
419 (**Figures 5b and 5c**).
420
421 Sources of uncertainties in this model are wall-slip parameters, contact angles at SCL_{up} and DCL,
422 as well as rheological fitting parameters. The sensitivities of slip coefficients and dynamic contact
423 angle on the predicted vacuum limits are shown in **Figure 6, S3, and S4 (S3 and S4 in Supporting**
424 **Information)** for fixed operating conditions. Changes of slip coefficient β within an order of
425 magnitude from its base value of 10^{-5} $m^3 \cdot N^{-1} \cdot s^{-1}$ lead to variation in vacuum limits of less than 10
426 Pa for the dilute ink, up to 100 Pa for the concentrated ink with Viscosity 1, or as much as 400 Pa
427 for the concentrated ink with Viscosity 2 at a web speed of 0.91 $m \cdot min^{-1}$ (3 $ft \cdot min^{-1}$). Thus,
428 increased viscosity results in higher sensitivity to slip coefficient. The vacuum window is invariant
429 with slip coefficient for small values of the slip coefficient (~10-6). However, the vacuum window

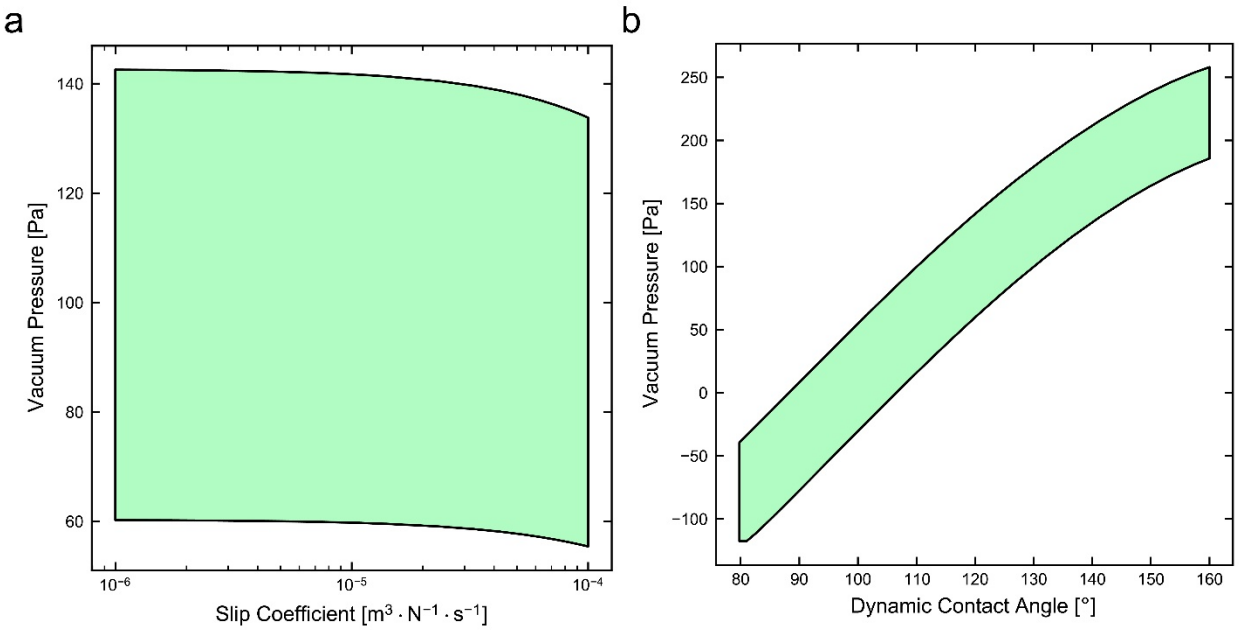

Figure 6. Sensitivity analysis of the a) slip coefficient, β, and b) dynamic contact angle (DCA) on the vacuum limits predicted for the dilute ink coating window calculated at a wet film thickness of 60 µm, a die-web gap of 150 µm, and a web speed of 0.91 $m \bullet min^{-1}$ (3 $ft \bullet min^{-1}$) using the Goma FEM.

is very sensitive to values for large values of the slip coefficient (~10-4). Thus, we choose the fixed value of slip coefficient at the transition between the regions of insensitivity and high sensitivity. Likewise, at the same coating speed, changes of dynamic contact angle within 40 ° from its base value of 120 ° leads to variation of the limit value of as much as 300 Pa. Additional factors not accounted for in the model are three-dimensional flow effects (flow of the ink that is not parallel to the web direction at the edges of the coating during steady uniform operation) and other non-Newtonian rheology behavior beyond shear-rate dependences of viscosity. The comparison of the modeled coating window with the experimental coating window indicates that these limitations are not significant for the conditions in this study.

3.2.2 Viscocapillary Model

The two-dimensional (2D) calculations by Goma described above incur moderate computational cost at roughly one day of computing on a single workstation per condition (each condition requiring computation of two vacuum limits for a series of web speeds). A significantly cheaper estimate of the vacuum limits can be obtained from the so-called viscocapillary lubrication model, wherein the coating bead flow is approximated to be unidirectional and the pressure a function solely of the coating direction (x-direction in **Figure 1b**). A modestly equipped personal laptop can compute the vacuum limits over a range of 50 web speeds in roughly one minute on the Matlab platform using the built-in ordinary differential equation (ODE) solver routine bvp5c as the workhorse solver.

The viscocapillary lubrication model for slot coater operability is described for Newtonian liquids by Higgins & Scriven[41] and for Carreau liquids by Koh et al.[42] We take generally the methodology of Koh et al. but with a different numerical method, the slightly more generalized Carreau-Yasuda

model (generalized from the Carreau model), and a modification of the viscosity used in the capillary number.

The vacuum pressure according to the viscocapillary model is determined by constructing a lubrication pressure chain from the upstream meniscus to the downstream meniscus. (Parameters used in this model are illustrated in the graphic in **Figure 1b**.) For the simplified case of parallel die-web gaps applicable to our process, the pressure difference between the ambient pressure P_0 and the pressure P_V in the upstream vacuum box is

$$P_0 - P_V = 1.34\left(\frac{\mu U}{\sigma}\right)^{2/3}\frac{\sigma}{t} + F_D\left(Q_f,U,H_0\right)L_D + F_U\left(Q_f,U,H_0\right)X_U + \frac{\sigma}{H_0}[\cos(\theta_U) + \cos(\theta_w)] \quad (3)$$

where typically the capillary number, $\frac{\mu U}{\sigma}$, is defined using the viscosity evaluated at the characteristic shear rate set by the web speed and downstream die-web gap, $\dot{\gamma} = U/H_0$. However, by comparison to 2D Goma results that do not need to make such an approximation, we find a better correspondence between the calculations when defining the capillary number with the gap H_0 replaced by the wet film thickness *t*. Further investigation is needed to determine the reason for this improvement.

$$\mu(\dot{\gamma}) = \mu\left(\frac{U}{t}\right) \quad (4)$$

The terms from left to right are

1. the Landau-Levich pressure drop across the downstream meniscus with viscosity evaluated from the generalized Newtonian model at the characteristic shear rate of the web speed divided by the wet film thickness. The wet film thickness is t and the surface tension of the liquid is σ.

2. the lubrication pressure drop across the (fully wetted) downstream lip of length L_D,
3. the lubrication pressure drop across the upstream coating bead of length X_U,
4. and the Laplace pressure drop across the upstream meniscus assuming a constant meniscus curvature (arc of circle) described by its contact angle with the web θ_w and the upstream die lip θ_U. The angles are chosen so that this term cancels out for simplicity.

The constant unknown pressure gradients F_D and F_U depend on the liquid rheology, the (constant, by the continuity **Equation 2a**) flow rate Q_f, the web speed U, and the die-web gap H_0. The flow rate and web speed are related to the target wet film thickness t via $Q_f = Ut$.

In the lubrication approximation, the momentum equation (**Equation 2b**) reduces to

$$0 = -F + \frac{\mathrm{d}}{\mathrm{d}x}\left(\mu(\dot{\gamma})\frac{\mathrm{d}u}{\mathrm{d}x}\right) \tag{5}$$

where the domain variable spans from the web at $x = 0$ to the die lip at $x = H$. The variable $u(x)$ is the flow-wise velocity profile in the slot, $\dot{\gamma}(x)$ is the shear rate profile, and F is the pressure gradient in the flow direction. The continuity statement is that the flow rate (integral of the velocity profile from wall to wall, Q_f) is constant.

A convenient (fully explicit) form of the lubrication equation upon application of the chain rule and some manipulations is

$$\begin{aligned} \frac{\mathrm{d}Q}{\mathrm{d}x} &= u \\ \frac{\mathrm{d}u}{\mathrm{d}x} &= \dot{\gamma} \\ \frac{\mathrm{d}\dot{\gamma}}{\mathrm{d}x} &= \frac{F}{\mu + \dot{\gamma}\frac{\mathrm{d}\mu}{\mathrm{d}\dot{\gamma}}} \end{aligned} \tag{6}$$

where $Q(x)$ is the cumulative flow rate (per unit trivial depth) such that the total flow is the difference of its boundary values, i.e., $Q_f = Q(H) - Q(0)$. Any generalized Newtonian viscosity model can be used as long as it is at least twice differentiable with respect to shear rate (the second derivative should be smooth if the boundary value problem (BVP) solver makes use of the sensitivities, which is typical).

The system of Eqs. (6) requires 4 boundary conditions, 3 for the ODEs and 1 extra for the unknown pressure gradient F. On the downstream gap with H_0

$$\begin{aligned} &Q(0) = 0 \\ &u(0) = U \\ &u(H_0) = 0 \\ &Q(H_0) = Q_f = Ut \end{aligned} \tag{7}$$

The first and last condition specify that the total flowrate (per unit depth) Q is that required to produce a wet film thickness t at web speed U, and the middle two conditions are simply the no-slip condition at the web and die lip. On the upstream gap, the total flow rate must be zero at steady state (upstream bead does not grow or shrink), such that

$$\begin{aligned} &Q(0) = 0 \\ &u(0) = U \\ &u(H_U) = 0 \\ &Q(H_U) = 0 \end{aligned} \tag{8}$$

Thus, to compute the vacuum pressure requires solving twice the set of Eqs. (6) for unknown F and asserted Q_f, once subject to boundary conditions Eqs. (7) for the downstream to give F_D, and again subject to boundary conditions Eqs. (8) for the upstream to give F_U. These BVPs with unknown parameter can be solved numerically using the bvp5c algorithm[43] as implemented in Matlab, where it is necessary to express all the derivatives explicitly (unlike the result of applying the product rule on Eq. (5), which would be implicit in the shear rate derivative). Although we

have presented the equations in dimensional form, we actually pose and solve the dimensionless equations, which are more convenient for programming and computation.

The viscocapillary model is expected to approximate the full 2D results well in the following limits:

1. Lubrication pressure drops across the coating beads under the die lips are better for infinitely narrow die-web gaps (large ratios of die lip land to die-web gap)
2. The Landau-Levich approximation is better for infinitesimally low capillary number
3. The upstream pressure drop approximation is better as the upstream meniscus takes a circular shape

The viscocapillary model operability window predictions for the dilute ink and the two viscosity profiles for the concentrated ink are shown in **Figure 5**. The viscocapillary predictions are closer to the Goma predictions for the dilute ink than for the concentrated inks, but in both cases the predictions deviate by no more than 100 Pa within the range of relevant line speeds, which is within the estimated uncertainty of the vacuum gauge. Thus, the viscocapillary model is a significantly cheaper (~1000 × faster on a business laptop vs Goma on a computer workstation) alternative to Goma FEM for PEMFC cathode ink operability window predictions within the experimental uncertainty of vacuum pressure measurements. Due to the computational cheapness of the viscocapillary model, we can quickly run a series of predictions showing how the coating window varies with die-web gap, H_0. As the gap increases from 1.5 to 5 times the coating thickness, the coating window strictly narrows; the maximum pressure decreases while the minimum pressure increases (**Figures 7, S5, and S6 (S5 and S6 in Supporting Information)**).

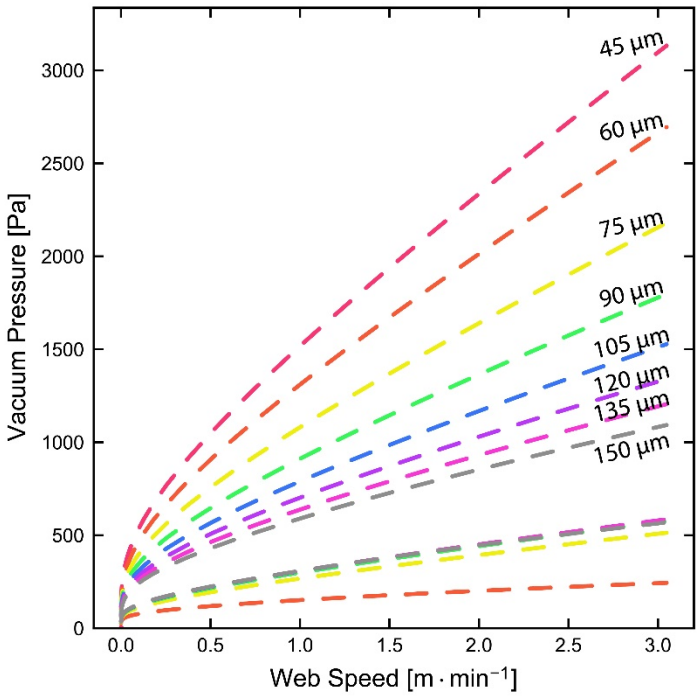

Figure 7. Viscocapillary model of the coating operability window for the concentrated ink, Viscosity 1 with a constant wet film thickness of 30 µm and die-web gaps ranging from 45 to 150 µm

As previously mentioned, μ_0, the viscosity plateau as the shear rate approaches 0, is unclear for the concentrated inks. Roughly speaking, we expect the low-shear-rate viscosity behavior differences to manifest at low coating speeds where the web speed divided by gap correspond to the shear rates of interest. Conservatively, the uncertainty in shear-viscosity is in the region below roughly 0.01 /s, which for 150 um gap translates to a web speed of 10^{-4} m·min^{-1}, which is well below speeds probed either in experiment or calculations, suggesting that predictions in the range of study should be insensitive to the μ_0 parameter. A sensitivity analysis (**Figures S7 and S8 in Supporting Information**) of the changes in operability window as a function of μ_0 confirms that the the operability window is insensitive to the choice of μ_0, even two orders of magnitude larger than the values in **Table 4**.

3.3 Roll-to-Roll Slot Die Coating of Catalyst Layers

To assess the validity of the coating windows predicted by the Goma and Viscocapillary models, we experimentally surveyed a range of vacuum levels and web speeds while R2R slot-die coating the dilute and concentrated inks. When coating the non-uniform MPL-GDL, a minimum coating gap, H_0, was set at 60 μm at the thickest position along the the MPL-GDL. Due to the variation in MPL-GDL thickness, the actual gap during the coating trial varied from 60 μm to ~150 μm. However, according to the model of how the coating window varies with H_0 (**Figures 7, S5, and S6 (S5 and S6 in Supporting Information)**), the coating parameters in the window for H_0 = 150 μm match closely with the windows for smaller gaps. Thus, we target the vacuum and line speed parameters in the narrow 150 μm gap coating window and expect that those parameters will work for the range of gaps during the MPL-GDL coating experiment. To validate the predicted coating window for H_0 = 150 μm, we experimentally determine the array of parameters that give a defect-free coating on aluminum foil, which has a much smaller thickness variation than the MPL-GDL.

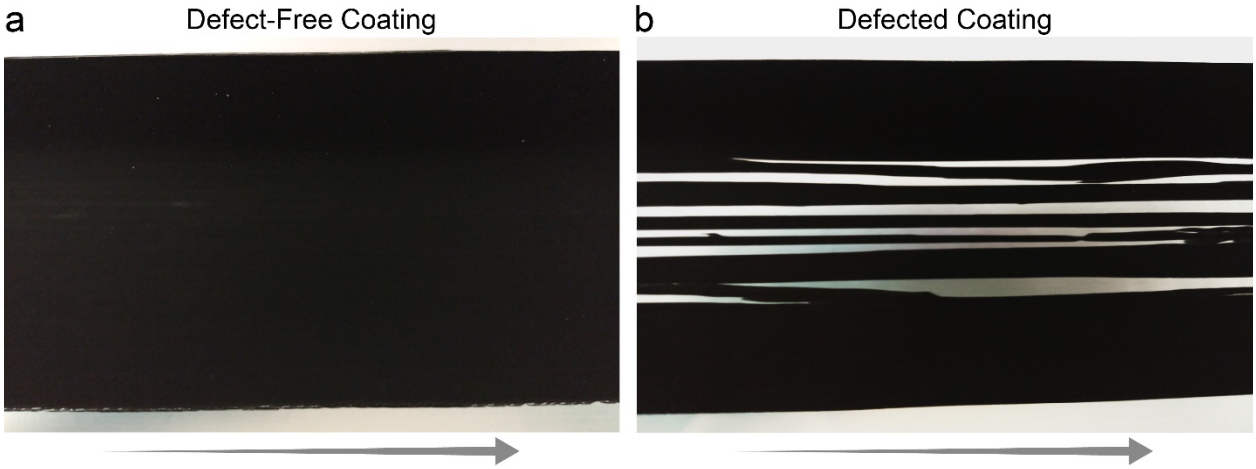

Figure 8. Optical images of a) defect-free and b) defected coatings of the concentrated ink on aluminum foil. The web direction is noted by the arrow beneath the pictures.

Due to the expense of the Pt-containing ink, only a horizontal (web speed) and vertical (vacuum pressure) line cut was tested out of the available coating space rather than a full array of points across the entire available coating space. To test the models without the added thickness variations and wetting uncertainties in the MPL-GDL, aluminum foil was used for most of the coating trials. A coating is considered "defect-free" if there are no obvious repeating macroscopic voids in the coating (**Figure 8a**). Coatings that showed obvious lines or dots were deemed "defected" (**Figure 8b**). After investigating the vacuum and line speed parameter space using the aluminum foil, a test coating near the center of the experimentally determined coating window was generated on the MPL-GDL to ensure that the coating parameters of the aluminum foil were valid on the PEMFC-relevant MPL-GDL.

Figure 5a shows the experimental coating results for the dilute ink on aluminum foil overlayed on the coating windows predicted by the two models. All points experimentally surveyed that lie within the theoretical coating window boundaries resulted in defect-free films while most points outside the the theoretical coating window boundaries produced defected coatings. The exception is the point at 2.7 $m \cdot min^{-1}$ and zero vacuum that lies below the theoretical coating window but

results in a defect-free coating. Therefore, we conclude that the actual high vacuum coating window boundary is not significantly different from the predicted boundary, but the models seem to overpredict the low vacuum limits for the dilute ink. Additionally, the same 60 μm wet thickness of the dilute ink gave a defect-free coating at 0-125 Pa vacuum from 0.6-2.7 m/min. web speed on the MPL-GDL. Thus, the predicted coating window also captures a region of defect-free coating for GDE production on the challenging hydrophobic and variable-thickness MPL-GDL substrate for the dilute ink.

For the concentrated ink, the agreement between experiment and the models worsens but still closely match in the case of the predictions based on Viscosity 1 (**Figures 5b and 5c**). Thus, the Viscosity 1 profile was selected as the best approximation for the concentrated ink in terms of ink preparation. Uncertainties in the model were discussed previously. The two most significant experimental uncertainties are the precision of the vacuum gauge and the rheological measurements. The pressure on the upstream vacuum gauge can only be read to the nearest 120 Pa (0.5 in. H_2O), represented by the error bars in **Figure 5**. Rheological uncertainties are discussed in section 3.1.4. The measured ink rheology can have a significant effect on the predicted operability window, especially for higher viscosity inks. There are also small uncertainties in the die-web gap set by feeler gauge. Neither the rheological nor the die-web gap uncertainties are included in the error bars in **Figure 5**.

Unlike the dilute ink, when we switched the substrate from aluminum foil to MPL-GDL the same set of coating parameters did not yield a defect-free coating on the MPL-GDL. In fact, we could not establish a defect-free coating at any combination of vacuum and line speed with the minimum

595 gap set to 60 μm. At these large gaps, the coating seeped into the vacuum box rather than being
596 applied to the substrate surface. Only when decreasing the actual gap (measured at the coating
597 bead location) to 45 μm was there a defect-free coating achieved. It is likely that the combination
598 of the high viscosity of the concentrated ink, the small wet thickness, t_{wet} of 30 μm, and the non-
599 wetting of the ink on the substrate restricts the die-web gap to smaller values. Though the
600 achievable 45 μm gap is smaller than the 150 μm target gap size, we still managed to keep the gap
601 at 1.5X the wet coating thickness. When coating thin films of inks with challenging rheology and
602 rapid solvent evaporation on a non-wetting substrate with variable thickness, the coating line may
603 need to be equipped with automatic adjustment of the gap while coating to compensate for the
604 deviation in substrate thickness along the coating direction.
605

606 # 4 Conclusions

607 The vacuum/web-speed slot-die coating window was predicted successfully at two concentrations
608 of PEMFC cathode catalyst ink with a two-dimensional FEM and a simplified viscocapillary
609 model. This is the first publication showing the application of slot die FEM models[34,38,39] or
610 viscocapillary models[41,42] to PEFMC cathode coatings. The dilute ink has a lower viscosity and a
611 narrower coating window while the concentrated ink's higher viscosity raises the vacuum
612 pressures needed for the coating window. The concentrated ink's shear viscosity profile was
613 especially sensitive to the rheological technique used, resulting in large changes to the resulting
614 coating window predictions. Future studies are needed to determine the effect of each component
615 of a rheological method and preparation on the measured shear viscosity curve. A primary
616 challenge of the experimental validation of the model proved to be the hydrophobicity of and

617 significant variation in thickness of the MPL-GDL substrate. Thus, most coating experiments were
618 performed on aluminum foil to eliminate the substrate effects. We were able to coat the dilute ink
619 on the MPL-GDL using vacuum levels and web speeds in the predicted operability window
620 without any issues, but we needed to decrease the die-web gap in order to coat the concentrated
621 ink on the MPL-GDL. Future studies in modeling will incorporate gap height perturbation due to
622 GDL-MPL substrate thickness variation by analyzing the transient effects on the resulting wet film
623 thickness[44] as well as the upstream meniscus location. Though the concentrated ink has a difficult-
624 to-achieve set of vacuum pressures that give a defect-free coating, the models' predictions allow
625 slot die operators to easily find these parameters, reducing wasteful material consumption when
626 experimentally searching parameters that lead to successful coatings. Additionally, enabling the
627 slot die coating of concentrated electrocatalyst inks for PEMFCs decreases drying energy
628 consumption, oven space and size required to dry the films, and solvent usage in the inks as well
629 as reducing labor hours and increasing throughput through R2R manufacturing. All of these
630 benefits contribute to cheaper and more sustainable production of PEMFC GDEs.
631

632 # 5 Acknowledgements

633 We gratefully acknowledge Alexander Kukay for the optical profilometer measurements and Dr.
634 Christopher Rulison at Augustine Scientific for optical tensiometer measurements. This
635 manuscript has been authored in part by UT-Battelle, LLC, under Contract No. DE-AC05-
636 00OR22725 with the U.S. Department of Energy (DOE) and sponsored by the Office of Energy
637 Efficiency and Renewable Energy (EERE) Advanced Manufacturing Office (AMO) (Program
638 Managers: David Hardy and Brian Valentine). Sandia National Laboratories is a multi-mission

laboratory managed and operated by National Technology and Engineering Solutions of Sandia, LLC., a wholly owned subsidiary of Honeywell International, Inc., for the U.S. Department of Energy's National Nuclear Security Administration under contract DE-NA0003525. A portion of this research was conducted at Saint-Gobain Research North America under contract DE-EE0008323. The U.S. government retains and the publisher, by accepting the article for publication, acknowledges that the United States Government retains a non-exclusive, paid-up, irrevocable, world-wide license to publish or reproduce the published form of this manuscript, or allow others to do so, for United States Government purposes. The Department of Energy will provide public access to these results of federally sponsored research in accordance with the DOE Public Access Plan (http://energy.gov/downloads/doe-public-access-plan).

6 References

(1) Mehta, V.; Cooper, J. S. Review and Analysis of PEM Fuel Cell Design and Manufacturing. *Journal of Power Sources*. 2003, pp 32–53. https://doi.org/10.1016/S0378-7753(02)00542-6.

(2) Arai, T.; Sato, S.; Morikawa, T. A Monolithic Device for CO<inf>2</Inf> Photoreduction to Generate Liquid Organic Substances in a Single-Compartment Reactor. *Energy Environ. Sci.* **2015**, *8* (7), 1998–2002. https://doi.org/10.1039/c5ee01314c.

(3) Whiston, M. M.; Azevedo, I. L.; Litster, S.; Whitefoot, K. S.; Samaras, C.; Whitacre, J. F. Expert Assessments of the Cost and Expected Future Performance of Proton Exchange Membrane Fuel Cells for Vehicles. *Proc. Natl. Acad. Sci. U. S. A.* **2019**, *116* (11), 4899–4904. https://doi.org/10.1073/pnas.1804221116.

(4) Energy, U. S. D. of. DOE Technical Targets for Fuel Cell Systems and Stacks for Transportation Applications https://www.energy.gov/eere/fuelcells/doe-technical-targets-fuel-cell-systems-and-stacks-transportation-applications (accessed Feb 26, 2020).

(5) Debe, M. K. Electrocatalyst Approaches and Challenges for Automotive Fuel Cells. *Nature* **2012**, *486* (7401), 43–51. https://doi.org/10.1038/nature11115.

(6) Mauger, S. A.; Neyerlin, K. C.; Yang-Neyerlin, A. C.; More, K. L.; Ulsh, M. Gravure Coating for Roll-to-Roll Manufacturing of Proton-Exchange-Membrane Fuel Cell Catalyst Layers. *J. Electrochem. Soc.* **2018**, *165* (11), F1012–F1018. https://doi.org/10.1149/2.0091813jes.

(7) García, R.; Steenberg, T.; Terkelsen, C.; Alfaro, S. M.; Avcioglu, G. S.; Vassiliev, A.; Primdahl, S.; Hjuler, H. A. Enabling Industrial Production of Electrodes by Use of Slot-Die Coating for HT-PEM Fuel Cells. *Int. J. Hydrogen Energy* **2019**, *44*, 12793–12801. https://doi.org/10.1016/j.ijhydene.2018.11.091.

(8) Beguin, A. E. Method of Coating Strip Material. 2681294, June 15, 1954.

(9) Cameron, E.; Wills, A. R. High Speed Coating Apparatus. 3413143, November 26, 1968.

(10) Krebs, F. C.; Fyenbo, J.; Jørgensen, M. Product Integration of Compact Roll-to-Roll Processed Polymer Solar Cell Modules: Methods and Manufacture Using Flexographic Printing, Slot-Die Coating and Rotary Screen Printing. *J. Mater. Chem.* **2010**, *20* (41), 8994–9001. https://doi.org/10.1039/c0jm01178a.

(11) Blankenburg, L.; Schultheis, K.; Schache, H.; Sensfuss, S.; Schrödner, M. Reel-to-Reel Wet Coating as an Efficient up-Scaling Technique for the Production of Bulk-Heterojunction Polymer Solar Cells. *Sol. Energy Mater. Sol. Cells* **2009**, *93* (4), 476–483. https://doi.org/10.1016/j.solmat.2008.12.013.

(12) Razza, S.; Castro-Hermosa, S.; Di Carlo, A.; Brown, T. M. Research Update: Large-Area Deposition, Coating, Printing, and Processing Techniques for the Upscaling of Perovskite Solar Cell Technology. *APL Mater.* **2016**, *4* (9), 091508. https://doi.org/10.1063/1.4962478.

(13) Espinosa, N.; García-Valverde, R.; Urbina, A.; Krebs, F. C. A Life Cycle Analysis of Polymer Solar Cell Modules Prepared Using Roll-to-Roll Methods under Ambient Conditions. *Sol. Energy Mater. Sol. Cells* **2011**, *95* (5), 1293–1302. https://doi.org/10.1016/j.solmat.2010.08.020.

(14) Zimmermann, B.; Schleiermacher, H. F.; Niggemann, M.; Würfel, U. ITO-Free Flexible Inverted Organic Solar Cell Modules with High Fill Factor Prepared by Slot Die Coating. *Sol. Energy Mater. Sol. Cells* **2011**, *95* (7), 1587–1589. https://doi.org/10.1016/j.solmat.2010.11.025.

(15) Wu, L. Y. L.; Kerk, W. T.; Wong, C. C. Transparent Conductive Film by Large Area Roll-to-Roll Processing. *Thin Solid Films* **2013**, *544*, 427–432. https://doi.org/10.1016/j.tsf.2013.02.087.

(16) Kim, S.; Kim, S. Y.; Chung, M. H.; Kim, J.; Kim, J. H. A One-Step Roll-to-Roll Process of Stable AgNW/PEDOT:PSS Solution Using Imidazole as a Mild Base for Highly Conductive and Transparent Films: Optimizations and Mechanisms. *J. Mater. Chem. C* **2015**, *3* (22), 5859–5868. https://doi.org/10.1039/c5tc00801h.

(17) Shin, K.; Park, J.; Lee, C. A 250-Mm-Width, Flexible, and Continuous Roll-to-Roll Slot-Die Coated Carbon Nanotube/Silver Nanowire Film Fabrication and a Study on the Effect of Anti-Reflective Overcoat. *Thin Solid Films* **2016**, *598*, 95–102. https://doi.org/10.1016/j.tsf.2015.12.004.

(18) Liu, D.; Chen, L.-C.; Liu, T.-J.; Chu, W.-B.; Tiu, C. Improvement of Lithium-Ion Battery

Performance by Two-Layered Slot-Die Coating Operation. *Energy Technol.* **2017**, *5* (8), 1235–1241. https://doi.org/10.1002/ente.201600536.

(19) Chen, L. C.; Liu, D.; Liu, T. J.; Tiu, C.; Yang, C. R.; Chu, W. B.; Wan, C. C. Improvement of Lithium-Ion Battery Performance Using a Two-Layered Cathode by Simultaneous Slot-Die Coating. *J. Energy Storage* **2016**, *5*, 156–162. https://doi.org/10.1016/j.est.2015.12.008.

(20) Mohanty, D.; Li, J.; Born, R.; Curt Maxey, L.; Dinwiddie, R. B.; Daniel, C. Non-Destructive Evaluation of Slot-Die-Coated Lithium Secondary Battery Electrodes by in-Line Laser Caliper and IR Thermography Methods †. *Anal. Methods* **2014**, *6*, 674. https://doi.org/10.1039/c3ay41140k.

(21) Schmitt, M.; Baunach, M.; Wengeler, L.; Peters, K.; Junges, P.; Scharfer, P.; Schabel, W. Slot-Die Processing of Lithium-Ion Battery Electrodes-Coating Window Characterization. *Chem. Eng. Process.* **2013**, *68*, 32–37. https://doi.org/10.1016/j.cep.2012.10.011.

(22) Jensen, J.; Dam, H. F.; Reynolds, J. R.; Dyer, A. L.; Krebs, F. C. Manufacture and Demonstration of Organic Photovoltaic-Powered Electrochromic Displays Using Roll Coating Methods and Printable Electrolytes. *J. Polym. Sci. Part B Polym. Phys.* **2012**, *50* (8), 536–545. https://doi.org/10.1002/polb.23038.

(23) Sandstrom, A.; Dam, H. F.; Krebs, F. C.; Edman, L. Ambient Fabrication of Flexible and Large-Area Organic Light-Emitting Devices Using Slot-Die Coating. *Nat. Commun.* **2012**, *3*, 1002. https://doi.org/10.1038/ncomms2002.

(24) Søndergaard, R. R.; Hösel, M.; Jørgensen, M.; Krebs, F. C. Fast Printing of Thin, Large Area, ITO Free Electrochromics on Flexible Barrier Foil. *J. Polym. Sci. Part B Polym. Phys.* **2013**, *51* (2), 132–136. https://doi.org/10.1002/polb.23189.

(25) Garner, S.; Glaesemann, S.; Li, X. Ultra-Slim Flexible Glass for Roll-to-Roll Electronic Device Fabrication. *Appl. Phys. A Mater. Sci. Process.* **2014**, *116* (2), 403–407. https://doi.org/10.1007/s00339-014-8468-2.

(26) Burdzik, A.; Stähler, M.; Friedrich, I.; Carmo, M.; Stolten, D. Homogeneity Analysis of Square Meter-Sized Electrodes for PEM Electrolysis and PEM Fuel Cells. *J. Coatings Technol. Res.* **2018**, *15* (6), 1423–1432. https://doi.org/10.1007/s11998-018-0074-3.

(27) Mauger, S. A.; Wang, M.; Cetinbas, F. C.; Dzara, M. J.; Park, J.; Myers, D. J.; Ahluwalia, R. K.; Pylypenko, S.; Hu, L.; Litster, S.; et al. Development of High-Performance Roll-to-Roll-Coated Gas-Diffusion-Electrode-Based Fuel Cells. *J. Power Sources* **2021**, *506*, 230039. https://doi.org/10.1016/j.jpowsour.2021.230039.

(28) Energy Information Administration (EIA). *Use of Energy in Industry*; 2019.

(29) Anastas, P. T.; Warner, J. C. *Green Chemistry: Theory and Practice: Paperback: Paul Anastas - Oxford University Press*; Oxford University Press: Oxford [England] ;;New York, 1998.

(30) Van Cleve, T.; Khandavalli, S.; Chowdhury, A.; Medina, S.; Pylypenko, S.; Wang, M.; More, K. L.; Kariuki, N.; Myers, D. J.; Weber, A. Z.; et al. Dictating Pt-Based Electrocatalyst Performance in Polymer Electrolyte Fuel Cells, from Formulation to Application. *ACS Appl. Mater. Interfaces* **2019**, *11* (50), 46953–46964. https://doi.org/10.1021/acsami.9b17614.

(31) Takahashi, S.; Mashio, T.; Horibe, N.; Akizuki, K.; Ohma, A. Analysis of the Microstructure Formation Process and Its Influence on the Performance of Polymer Electrolyte Fuel-Cell Catalyst Layers. *ChemElectroChem* **2015**, *2* (10), 1560–1567. https://doi.org/10.1002/celc.201500131.

(32) Schunk, P. R.; Rao, R. R.; Chen, K. S.; Labreche, D. A.; Sun, A. C.-T.; Hopkins, M. M.; Moffat, H. K.; Roach, R. A.; Hopkins, P. L.; Notz, P. K.; et al. *GOMA 6.0 : A Full-Newton Finite Element Program for Free and Moving Boundary Problems with Coupled Fluid/Solid Momentum, Energy, Mass, and Chemical Species Transport : User's Guide*; Albuquerque, 2013. https://doi.org/10.2172/1089869.

(33) Fowkes, F. M. Attractive Forces at Interfaces. *Ind. Eng. Chem.* **1964**, *56* (12), 40–52. https://doi.org/10.1021/ie50660a008.

(34) Sartor, L. Slot Coating: Fluid Mechanics and Die Design, University of Minnesota, 1990.

(35) Ding, X.; Liu, J.; Harris, T. A. L. A Review of the Operating Limits in Slot Die Coating Processes. *AIChE J.* **2016**, *62* (7), 2508–2524. https://doi.org/10.1002/aic.15268.

(36) Khandavalli, S.; Park, J. H.; Kariuki, N. N.; Myers, D. J.; Stickel, J. J.; Hurst, K.; Neyerlin, K. C.; Ulsh, M.; Mauger, S. A. Rheological Investigation on the Microstructure of Fuel Cell Catalyst Inks. *ACS Appl. Mater. Interfaces* **2018**, *10* (50), 43610–43622. https://doi.org/10.1021/acsami.8b15039.

(37) Romero, O. J.; Suszynski, W. J.; Scriven, L. E.; Carvalho, M. S. Low-Flow Limit in Slot Coating of Dilute Solutions of High Molecular Weight Polymer. *J. Nonnewton. Fluid Mech.* **2004**, *118* (2–3), 137–156. https://doi.org/10.1016/j.jnnfm.2004.03.004.

(38) Malakhov, R.; Tjiptowidjojo, K.; Schunk, P. R. Mechanics of the Low-Flow Limit in Slot-Die Coating with No Vacuum. *AIChE J.* **2019**, *65* (6), e16593. https://doi.org/10.1002/aic.16593.

(39) Carvalho, M. S.; Kheshgi, H. S. Low-Flow Limit in Slot Coating: Theory and Experiments. *AIChE J.* **2000**, *46* (10), 1907–1917. https://doi.org/10.1002/aic.690461003.

(40) Sackinger, P. A.; Schunk, P. R.; Rao, R. R. *A Newton-Raphson Pseudo-Solid Domain*

*Mapping Technique for Free and Moving Boundary Problems: A Finite Element Implementation**; 1996; Vol. 125.

(41) Higgins, B. G.; Scriven, L. E. Capillary Pressure and Viscous Pressure Drop Set Bounds on Coating Bead Operability. *Chem. Eng. Sci.* **1980**, *35* (3), 673–682. https://doi.org/10.1016/0009-2509(80)80018-2.

(42) Koh, H. J.; Kwon, I.; Jung, H. W.; Hyun, J. C. Operability Window of Slot Coating Using Viscocapillary Model for Carreau-Type Coating Liquids. *Korea Aust. Rheol. J.* **2012**, *24* (2), 137–141. https://doi.org/10.1007/s13367-012-0016-z.

(43) Kierzenka, J.; Shampine, L. F. A BVP Solver That Controls Residual and Error. *J. Numer. Anal. Ind. Appl. Math.* **2008**, *3* (1–2), 27–41.

(44) Maza, D.; Carvalho, M. S. Transient Response of Two-Layer Slot Coating Flows to Periodic Disturbances. *AIChE J.* **2015**, *61* (5), 1699–1707. https://doi.org/10.1002/AIC.14734.